A numerical study of geometry dependent errors in velocity, temperature, and density measurements from single grid planar retarding potential analyzers

R. L. Davidson,[1] G. D. Earle,[1] J. H. Klenzing,[2] and R. A. Heelis[1]
[1]*William B. Hanson Center for Space Sciences, The University of Texas at Dallas, 800 W. Campbell Road, WT15, Richardson, Texas 75080, USA*
[2]*Space Weather Laboratory/Code 674, Goddard Space Flight Center, Greenbelt, Maryland 20771, USA*

(Received 15 April 2010; accepted 7 June 2010; published online 9 August 2010)

Planar retarding potential analyzers (RPAs) have been utilized numerous times on high profile missions such as the Communications/Navigation Outage Forecast System and the Defense Meteorological Satellite Program to measure plasma composition, temperature, density, and the velocity component perpendicular to the plane of the instrument aperture. These instruments use biased grids to approximate ideal biased planes. These grids introduce perturbations in the electric potential distribution inside the instrument and when unaccounted for cause errors in the measured plasma parameters. Traditionally, the grids utilized in RPAs have been made of fine wires woven into a mesh. Previous studies on the errors caused by grids in RPAs have approximated woven grids with a truly flat grid. Using a commercial ion optics software package, errors in inferred parameters caused by both woven and flat grids are examined. A flat grid geometry shows the smallest temperature and density errors, while the double thick flat grid displays minimal errors for velocities over the temperature and velocity range used. Wire thickness along the dominant flow direction is found to be a critical design parameter in regard to errors in all three inferred plasma parameters. The results shown for each case provide valuable design guidelines for future RPA development.
 [doi:10.1063/1.3457931]

I. INTRODUCTION

Since the mid-20th century planar retarding potential analyzers (RPAs) have been one of the most reliable instruments for *in situ* plasma measurements. RPAs have been included on many high profile satellite missions including Sputnik 3,[1] Atmospheric Explorer,[2] Dynamics Explorer,[3] The Defense Meteorological Satellite Program,[4] and The Communication/Navigation Outage Forecast System.[5] Data from RPAs are essential for studies of fundamental ionospheric plasma phenomena such as equatorial spread F,[6] the Equatorial Anomaly,[7] polar convection patterns,[8] and magnetic storm responses.[9]

The conceptual workings of the RPA are relatively simple to understand. As shown in Fig. 1, a RPA consists of a grounded aperture, open to a plasma, followed by one or more permeable biased planes (including a retarding plane or planes and a suppressor plane) followed by a solid plate collector.[10] The retarding plane is swept over a range of voltages creating an "energy hill" that incoming ions must climb in order to reach the collector. As the voltage on the retarding plane increases, a smaller portion of the ions have enough energy to climb the hill and be counted at the collector as a current. This current-voltage (I-V) characteristic is related to the velocity distribution of the ions. From this I-V curve multiple plasma characteristics can be extracted including plasma component densities, temperature, and velocity normal to the retarding plane.

Departures from the ideal case must be considered in order to accurately determine those parameters using real instruments. In real instruments fine mesh grids must be used to approximate the ideal permeable retarding plane(s). These grids introduce small perturbations in the potential distribution within the instrument and distort the energy hill the ions experience. For example, the potential in-between grid wires is slightly less than the potential applied to the grid itself. The potential depression between grid wires also leads to the "lensing" of particles, focusing them into the depression and away from the wires. This allows ions that would otherwise be excluded to leak through the retarding grid. The excess current this creates introduces errors in the inferred plasma parameters listed above. Real retarding grids also have some depth associated with the thickness of the grid wires. This causes particles with sufficiently large transverse velocities to be collected by the retarding grid instead of the collector. All of these effects combine to alter the I-V characteristic in ways not predicted by the standard theory and introduce errors in the plasma parameters inferred from RPA measurements.

Earlier work has examined some of the effects of real grids on inferred plasma parameters by Chao *et al.*[11,12] and Klenzing *et al.*[13,14] The work presented here builds on those efforts by taking into account the geometry of the retarding grid as well. In the earlier studies by Klenzing and Chao a truly flat grid is assumed. While this is a reasonable and computationally simple approximation, in reality most RPAs flown to date have used a woven grid. Flat grids manufactured using electroforming processes have only recently become available. A woven grid, on average, has more depth than a flat grid and thus the grid loss effect should be exaggerated for such a geometry. The potential perturbations in a

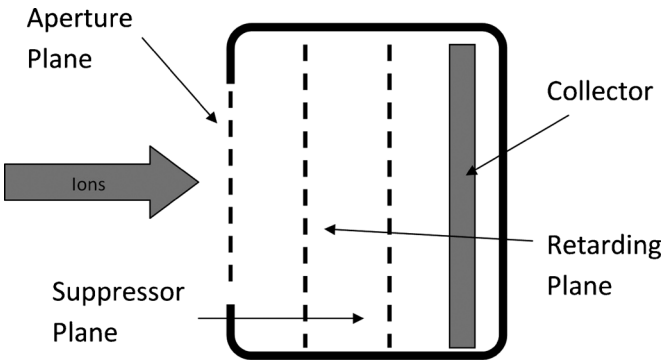

FIG. 1. Conceptual cut-away drawing of a RPA showing internal biased planar surfaces.

woven grid are nonuniform as well, possibly leading to unexpected leakage behavior. The focus of the present study is to examine these deleterious effects, particularly how they impact plasma temperature, velocity, and density estimates in the ionospheric medium.

II. IDEAL THEORY

In general, the current measured at the collector by an ideal planar RPA moving supersonically with respect to a plasma is given by

$$I(\varphi_{RV}) = qAN_0 \int_{v_x=-\infty}^{\infty} \int_{v_y=-\infty}^{\infty} \int_{v_z=0}^{\infty} \chi(v,\varphi_{RV}) v_z D(v) dv, \tag{1}$$

where q is the fundamental charge, A is the area of the aperture (it is assumed that the aperture is smaller than the collector), N_0 is the ion density, v_x and v_y are velocity components in the plane of the aperture, v_z is the velocity component normal to the aperture plane (or ram velocity), $\chi(v,\varphi_{RV})$ is the transmission function, and $D(v)$ is the normalized three dimensional velocity distribution of the ions outside the instrument. The velocities in this expression are all measured in the rest frame of instrument (the moving spacecraft). Velocity in the normal direction is integrated from 0 because only particles that enter the instrument can be collected. For a plasma that has had sufficient time to thermalize, it is assumed that the distribution will be a drifting Maxwellian. The transmission function is simply a step function that allows particles with "ram energy" ($\frac{1}{2}mv_z^2$, m being mass) greater than the potential barrier presented by the retarding grid to pass through to the collector, while those with less energy will be rejected. This integral is analytically solvable, yielding a current for a given retarding potential in a single ion species plasma described by

$$I(\varphi_{RV}) = \frac{qAN_0\chi_0 v_{\text{ram}}}{2}\left[1 + \text{erf}(\kappa) + \frac{v_{\text{th}}}{v_{\text{ram}}\sqrt{\pi}} e^{-\kappa^2}\right], \tag{2}$$

where

$$\kappa = \frac{\left(v_{\text{ram}} - \sqrt{\frac{2q\phi_{RV}}{m}}\right)}{\sqrt{2k_BT/m}}. \tag{3}$$

Here mass is m, T is temperature, k_B is the Boltzmann constant, and χ_0 is the optical transparency of the retarding plane (grid).[1] For more than one species the current is simply the sum of terms resembling the right side of Eq. (2) with appropriate masses, thermal velocities, and densities for each ion species. Equation (2) describes the I-V characteristic in an ideal RPA; it is used along with nonlinear least-squares curve fitting techniques to extract ion temperature, density, and velocity normal to the retarding plane. In the equations above it is assumed that the instrument ground potential is the same as the plasma potential, but in practice the spacecraft can retain a charge as it moves through the plasma, and thus the applied voltage is shifted by some constant. This spacecraft potential can also be inferred from the RPA I-V characteristic, but for simplicity spacecraft charging considerations are ignored here.

In the ideal equation the optical transparency of the grid is taken into account but leakage and grid loss effects are ignored. There is no known analytical solution using real grids, so a numerical approach must be utilized. Such an approach is employed for this work and described below.

III. NUMERICAL SIMULATION

The simulations are conducted using SIMION® v. 8.0 ion optics software[15] to examine three different grid types, as illustrated in Fig. 2. The grid geometries are defined in a straightforward way wherein a three dimensional cubic set of points represents a volume in space, where some points are designated as electrode points to form the grid and the rest are left as free space points. Electrode points are given a set voltage that does not change, corresponding to surfaces in a real instrument to which regulated voltages are applied and maintained. Free space points are assigned voltages that are obtained through an iterative relaxation method technique.[16] Equipotential contours showing the potential map inside a single grid cell for each geometry can be seen in Fig. 3. The boundaries are left floating because the voltage at the boundaries can be instrument specific. This does not perturb the trajectories because the particles are introduced far from the boundaries and never travel close enough to a boundary to be affected by unwanted fringing fields, as can be seen in Fig. 4. An ideal, flat, perfectly permeable plane is used for both the aperture grid and the suppressor grid. Since the gradient in the voltage is largest at the retarding grid, it is assumed that the largest departures from the ideal equation will occur at that location, thus the other grids are left as ideal. In real instruments the suppressor grid has a negative potential and serves to turn back photoelectrons emitted from the collector plate as well as to screen out ambient electrons so that only ions reach the collector. Electrons are not included in the simulation and in order to isolate the effects of having a single biased gird the suppressor plane is left grounded. The omission of a voltage on the suppressor plane will decrease the gradient in the potential at the retarding grid and reduce

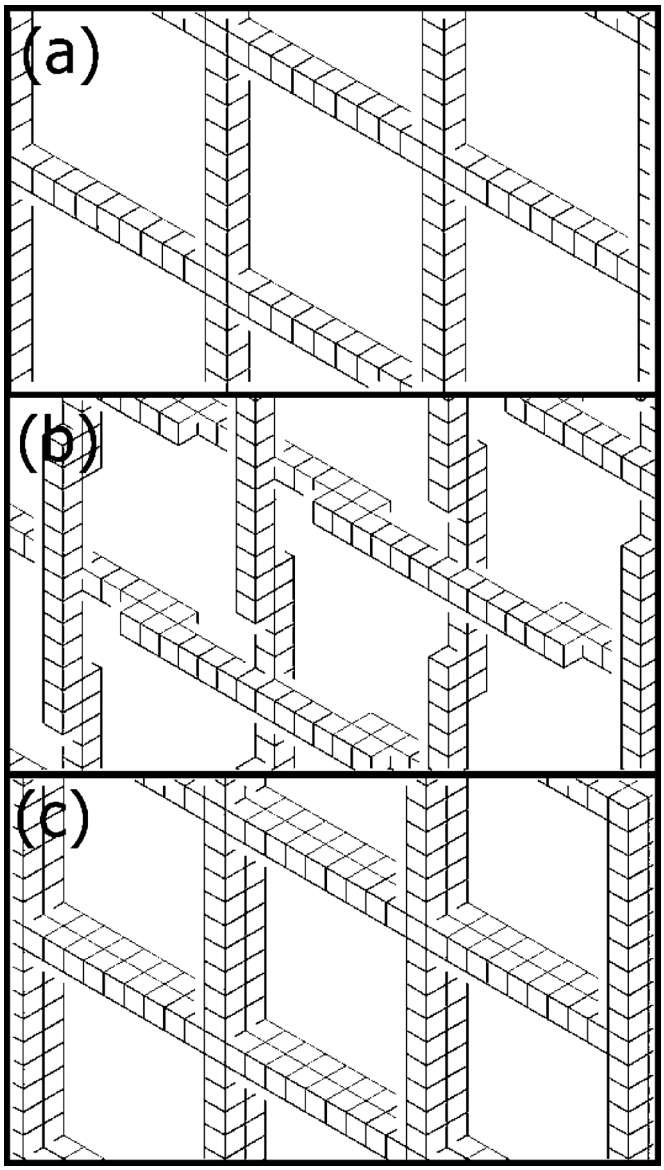

FIG. 2. Detailed view of the three grid geometries studied. Panel (a) shows the flat grid, panel (b) shows the woven grid model, and panel (c) shows the double thick flat grid. All grids are defined using SIMION®.

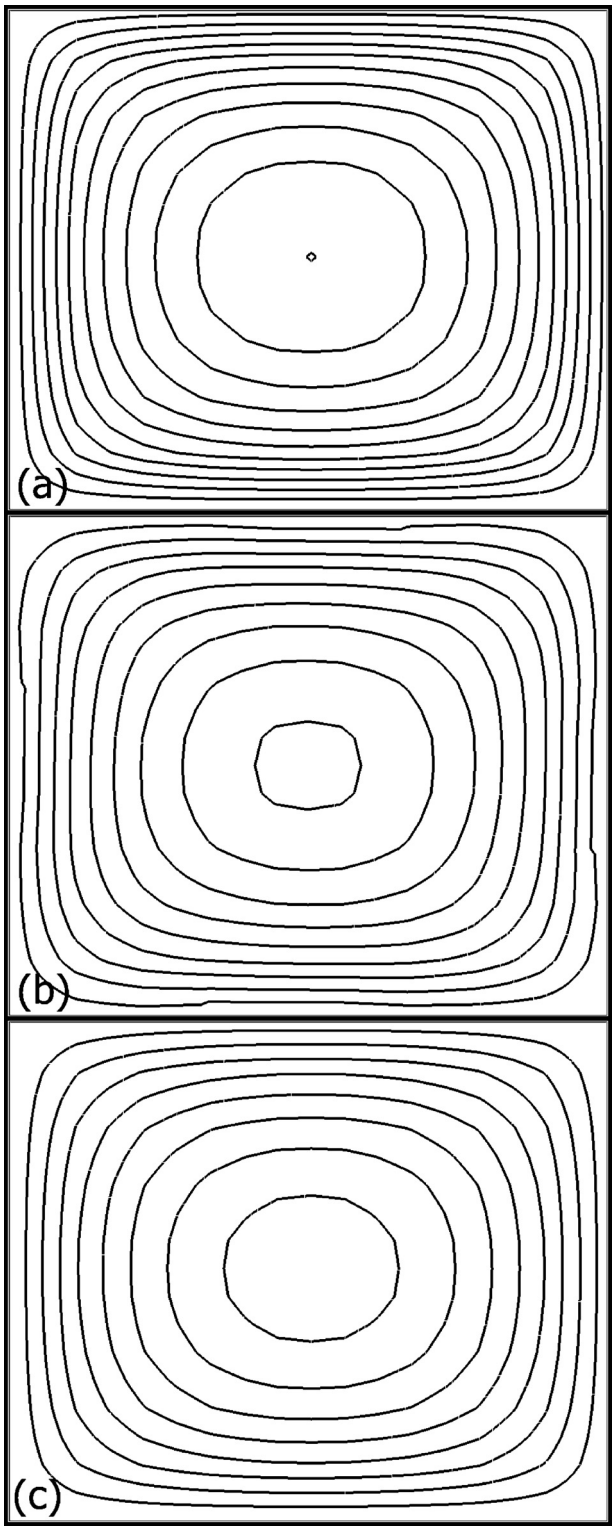

FIG. 3. A view of equipotential lines inside a single grid cell for flat (a), woven (b), and double thick (c) grid geometries. In each case the grid itself was held at 10 V. The outermost contour line is at 9.975 V and each successive line is spaced at 0.025 V intervals. Notice that the single thick grid shows the largest depletion and that the woven grid has distinct kinks in the outmost contour line.

the magnitude of some of the errors derived from the simulation when compared to a real instrument of standard design. The retarding grid is made using 1 mil wires with 100 wires/in. and a spacing between grids of 100 times the wire thickness. The flat grid is a relatively straightforward geometry, as is the double thick flat grid (simply having twice the depth of the flat grid). The woven grid is approximated by using alternating sections of straight square wires. This somewhat crude approximation is necessary to achieve a large enough grid size to enable the computation while still managing to capture the essential feature of the woven grid, the fact that it is structured in three dimensions and is on average slightly deeper than the flat grid.

Once the potential distribution is known for a given grid geometry and retarding voltage, a distribution of N_2 ions is created just outside of the aperture plane. Nitrogen is used in order to provide results that will be comparable to independent laboratory tests, which will be the subject of a separate paper. These particles are randomly produced to fit a three dimensional Gaussian distribution in velocity, with the variances determined by the temperature of the assumed distri-

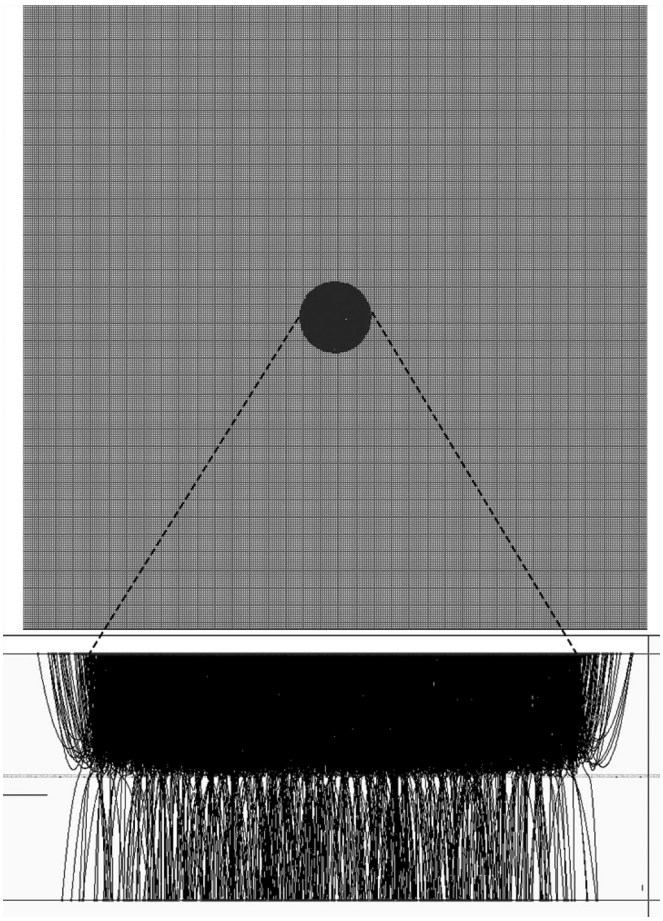

FIG. 4. A normal incidence view of the aperture plane, showing the small area in which particles are introduced, and a magnified cross-section view of typical particle trajectories at a retarding potential near the mean particle energy.

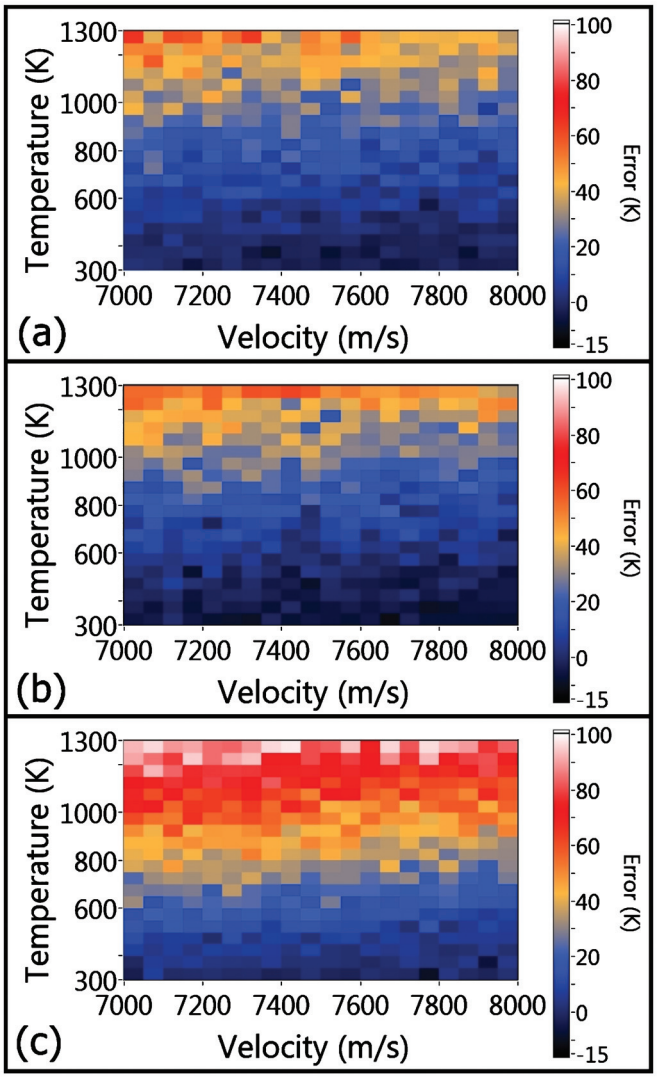

FIG. 5. (Color) Temperature errors calculated from I-V curve fitting as a function of the temperature and velocity component normal to the aperture plane of the incident particle distribution for flat, woven, and double thick flat grid geometries [panels (a), (b), and (c), respectively]. A positive error corresponds to the fit producing a value larger than the input value.

bution. All velocities parallel to the aperture plane are set to a mean of zero to limit the set of independent variables involved. The particles' trajectories are calculated through the potential distribution using the proprietary SIMION™ Runge–Kutta method.[17] A sample set of ion trajectories is presented in Fig. 4 for a retarding voltage near the mean energy of the ram distribution. For a given input temperature and velocity each ion's position and velocity vectors are recorded at the beginning and end of its flight. This process is repeated for each retarding voltage (0–14 V in 0.5 V steps). These data are then analyzed and particles that pass through the retarding grid and the repelling plane are used to construct a simulated I-V curve (with total particle count as a proxy for current). These I-V curves are then fit using a least-squares Levenburg Marquardt[18] curve fitting routine and the ideal model [Eq. (2)]. From these fits and the known input parameters, errors in temperature and the component of velocity normal to the aperture plane are determined for each set of inputs. An additional set of errors is calculated by comparing the total flux of particles that arrive at the collector to the flux expected due to the retarding grid bias and the optical transparency factor in Eq. (2).

IV. DATA PRESENTATION: ERRORS IN INFERRED PARAMETERS

Input temperature ranges from 300 to 1250 K in 50 K steps, and input velocity ranges from 7000 to 7950 m/s in 50 m/s steps are used to create a total of 400 sets of input parameters for each grid geometry. These ranges correspond to realistic values for plasmas encountered in low earth orbit, where RPAs are commonly used. Errors in temperature as a function of input temperature and velocity for all three geometries can be seen in Fig. 5. Errors in velocity as a function of input temperature and velocity for all three geometries are shown in Fig. 6. Errors in density are presented in Fig. 8. Errors in composition are not studied because we assume a single species for simplicity, and to make the grid effects on the other inferred parameters unambiguous. All errors are calculated by subtracting the known input parameter from the inferred fit parameter, so positive errors indi-

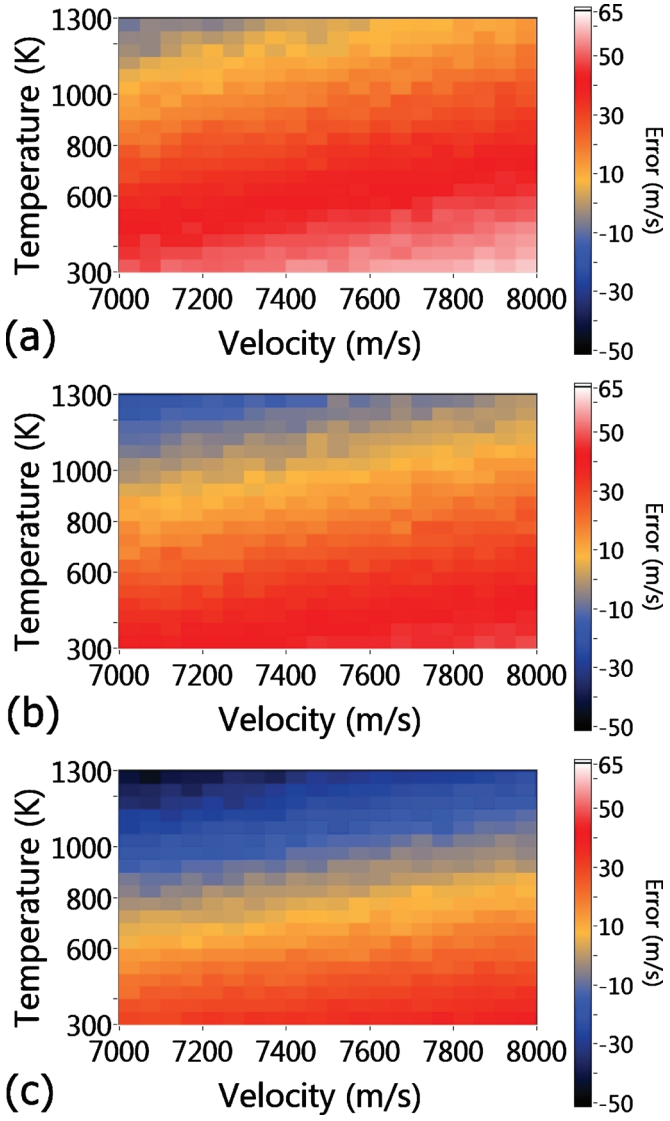

FIG. 6. (Color) Errors in the velocity component normal to the aperture calculated from I-V curve fitting as a function of the temperature and velocity component normal to the aperture plane of the incident particle distribution for flat, woven, and double thick flat grid geometries [panels (a), (b), and (c), respectively]. A positive error corresponds to the fit producing a value larger than the input value.

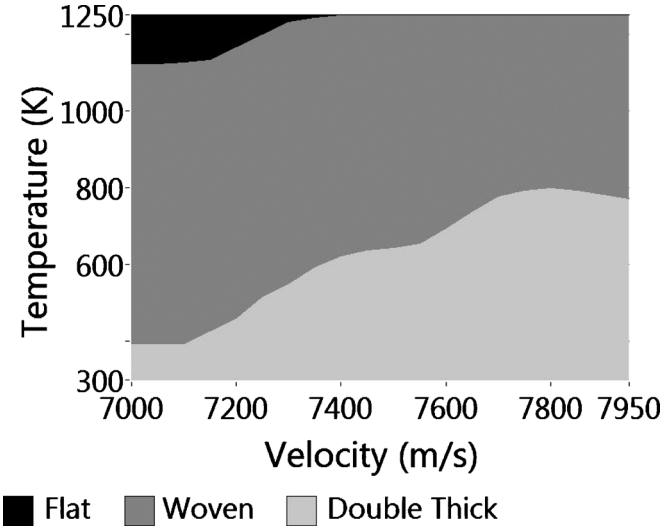

FIG. 7. Regions of velocity errors with a magnitude of less than 30 m/s for each grid geometry.

cate that the fit is larger than the ideal equation predicts it should be.

The errors in temperature shown in Fig. 5 are somewhat noisy due to the finite number of particles and the discrete voltage steps used in the simulation. Errors inherent in the fitting process are unavoidable, but low residuals obtained for the fits suggest that this error is small when compared with the errors produced by the grid geometries. In spite of these noise effects a clear positive correlation between the input temperature and the fitted temperature errors can be seen in all three cases. Input velocity has little effect on the temperature errors. Overall, the three geometries show very similar qualitative errors. When examined quantitatively, however, some differences emerge. The flat grid and double flat grid geometries have very similar minimum errors, about −10 K, at the lowest input temperature. The maximum error is larger by about 50% in the double thick case when compared with the single thick case (85 versus 45 K). The woven grid temperature errors very closely resemble those for the flat grid, having similar structure and error ranges.

The errors in velocity normal to the aperture plane also show very similar qualitative structure in all three geometries in Fig. 6. Input velocity is positively correlated with velocity errors, while input temperature is negatively correlated with velocity errors. Again, the magnitudes of the errors in each case differ considerably. The single flat grid has a range of errors between 24 and 47 m/s, the woven grid has errors between 12 and 36 m/s, and the double thick grid has errors between −12 and 25 m/s. This ordering exactly reflects the average depth of the grids. In each case there is a range of input parameters that lead to very small errors. For the given inputs this area is largest for the double thick case, smallest for the single thick case, and the woven grid falls between the other two.

Figure 7 shows the inputs for each geometry that produce small velocity errors (less than 30 m/s in magnitude). These low error regions show the conditions under which a certain grid geometry is most accurately able to measure velocity normal to the aperture plane. All three geometries show a stripe across the range of inputs that has a positive slope of similar magnitude. The small error regions overlap significantly. The flat grid has small errors for relatively smaller velocities and higher temperatures than the other two geometries. The double thick grid shows small errors for all input temperatures and velocities and temperatures simulated. The woven grid's small error region falls in between the regions for the other two grid geometries.

The errors in density are all negative and are presented in Fig. 8. All three geometries show a strong negative correlation between temperature and density error and a less pronounced positive correlation between input velocity and density error. The single flat grid shows the smallest errors (between −0.41% and −1.55%), followed by the woven grid (between −0.55% and −1.90%), and the double thick flat

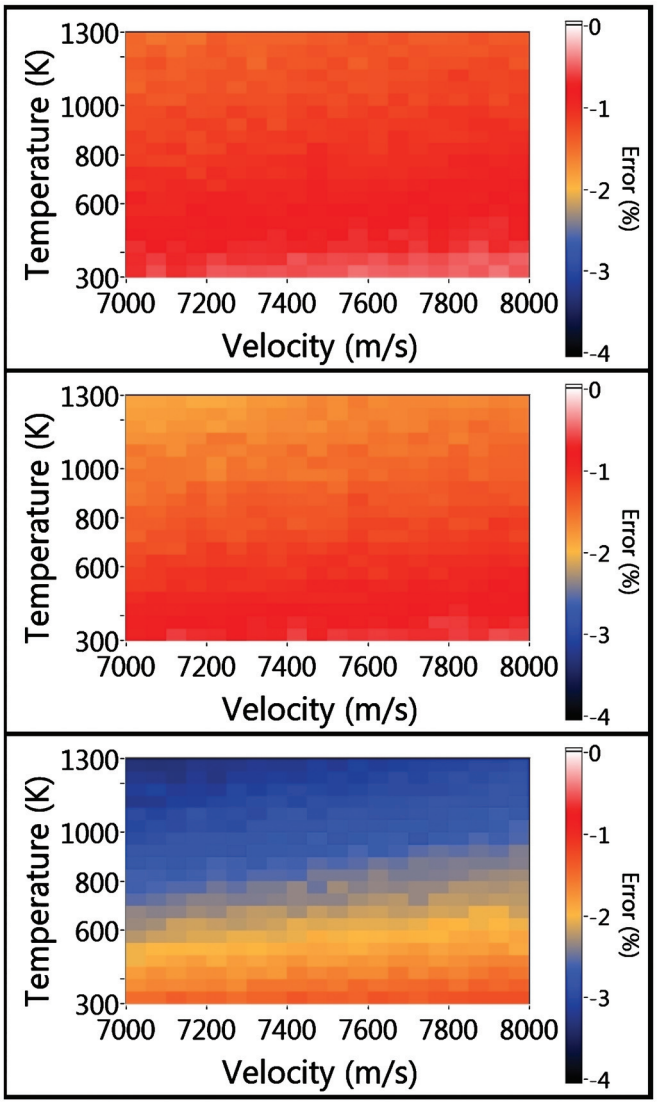

FIG. 8. (Color) Density errors calculated from I-V curve fitting as a function of the temperature and velocity component normal to the aperture plane of the incident particle distribution for flat, woven, and double thick flat grid geometries [panels (a), (b), and (c), respectively]. A positive error corresponds to the fit producing a value larger than the input value. Errors are expressed as a percent of the total flux expected.

grid (between −1.27% and −3.34%), respectively. All the density errors increase drastically as the grid becomes thicker.

V. DISCUSSION

The similar features common to all three geometries are evident in all of the inferred plasma parameters. The structure in the errors in each parameter is fundamentally caused by the use of a real grid instead of an ideal permeable plane. The differences between grid geometries, for the most part, only influence the magnitude of these errors. To explain the overall similarity for each set of plots as well as the distinct differences arriving for the different geometries, the causes of each type of error must be examined.

Temperature is a measure of the width of the distribution and thus the average magnitude of the slope of the I-V curve. As the temperature increases the distribution widens, and the average I-V slope decreases. At higher temperatures the average cross track speed from thermal motion increases, and it becomes increasingly likely that particles will impact the side of a grid wire. As the voltage on the retarding grid is increased, however, the transverse electric field between the wires also increases. These electric fields tend to focus incoming particles between the wires, and thus particles are less likely to impact grid wires as the voltage on the retarding grid is increased. These two effects oppose each other, but, in general, do not cancel out. At low retarding voltages thermal effects dominate and less current is allowed to the collector than is expected. At higher voltages ions are pushed in-between the grid wires by transverse electric fields and more current than would otherwise be expected is allowed to reach the collector. This asymmetric current effect tends to broaden the I-V curve and lead to the temperature errors seen in Fig. 5. The velocity of the particles normal to the aperture has very little effect on temperature errors because velocity effects are mostly independent of voltage, and thus do not sharpen or broaden the I-V curve noticeably. When the input temperature is very low (~300 K) the ions have very small velocities in the plane of the grid and thus very closely resemble the ideal situation. At high temperatures the I-V curve is broadened leading to a positive temperature error. All of these expected behaviors are captured in the simulations for all three geometries and quantified in Fig. 5.

The differences in magnitude and range of the temperature errors seen in the three geometries can be explained by considering the average wire depth. At low temperatures there is very little thermal spread, making wire depth of little importance. At high temperatures, the depth of the grid results in a larger number of ions being lost than would be expected, leading to a larger error. At any given point (excluding the intersection of wires) the woven grid is composed of a wire with single thickness, much like the single thick grid. This fact explains the similarity in the errors produced by those geometries. The double thick grid produces considerably larger temperature errors than the other two geometries. Our simulation suggests that wire depth appears to be a key factor in influencing temperature errors.

An error in the velocity estimate arises when the I-V curve is shifted to either the right or the left relative to the appropriate shift for its energy level. The space between the grid wires leads to potential depletions in the grid cells so that, on average, particles see a smaller voltage than the potential applied to the retarding grid. This effect leads to a leakage through the retarding grid of particles whose energy would be insufficient in the ideal case. This happens at a relatively consistent ratio for any given retarding voltage and thus tends to shift the I-V curve to the right because higher potentials are required to achieve the desired energy filtering. This effect increases with velocity simply because energy varies as velocity squared. The effects of temperature are the same as described above; namely, transverse velocities cause particles to impact the sides of grid wires, leading to reduced collector currents. These two effects partially offset each other, and thus a balance is reached in certain regions where the two effects nearly cancel each other out. At low veloci-

ties and high temperatures, grid loss dominates, giving a negative velocity error. At high velocities and low temperatures, the leakage effect takes over and positive velocity errors are observed. All of these features are shared by the three geometries and are quantified in Fig. 6.

The different geometries, while showing the same general pattern, differ considerably in the magnitude of their respective velocity errors. The increasing depth of the grid increases the loss of particles to the grid wires for the simple reason that grid depth translates into larger transverse grid area. Grid depth also reduces the potential depletion between grid wires and increases the average maximum potential the incoming particles experience (although it is still smaller than the potential placed on the grid itself). Increased grid depth thus increases the grid loss while simultaneously decreasing the leakage effect. This can clearly be seen by comparing the different grid geometries in Fig. 6. For a certain range of inputs, grid loss and particle leakage balance to produce very small errors. This balance occurs at relatively lower temperatures for grids with greater depth.

The inputs for which a certain grid geometry performs optimally for velocity measurements (as shown in Fig. 7) reveal that there is no clear "best" geometry for velocity measurements. Each geometry should be able to most accurately measure velocity for a different range of input parameters. For the inputs chosen for this study the double thick flat grid has smaller velocity errors than the other two geometries. The other geometries most likely have similar small error trenches at higher temperatures or at lower velocities than those simulated here. This suggests that to minimize errors caused by grid geometry some knowledge of the plasma input parameters to be measured would be of great importance in selecting the best geometry. The temperature range considered here is appropriate for the bottomside ionosphere and/or nighttime conditions. However, given the banded structure of Fig. 7, it seems appropriate to infer that the choice of grid design should differ depending on the temperature range of the plasma under study.

It is possible to qualitatively extend these results to apply to typical ionospheric conditions. The ionosphere is mainly composed of atomic oxygen, hydrogen, and helium, all of which have less mass than molecular nitrogen. Temperatures also typically reach values of up to a few thousand degrees Kelvin. For these reasons, the average transverse velocities encountered in the ionosphere would be large compared to the transverse particle velocities simulated here. The grid loss effect would therefore be much more prominent than it is in the errors presented here. This would suggest that a flat or woven grid would be superior for all three measurements in typical ionospheric conditions.

The total plasma density is obtained mainly from the magnitude of the current measured when the retarding voltage is zero. As such the main factor in determining the density is simply the true transparency of the grid to incoming particles. The ideal equation only considers the optical transparency, ignoring particles that hit the sides of the grid wires. The small number of particles lost to the grid at zero retarding voltage and not accounted for in the ideal equation account for nearly all of the density errors. This error is related to the ratio of the normal velocity to the transverse velocity for a given particle, thus the magnitude of the error increases with temperature and decreases with velocity. This behavior is observed in all three geometries and is detailed in Fig. 8.

Since density is determined by a part of the curve where potential is unimportant, errors in the inferred plasma density are caused simply by geometrical considerations. The number of particles collected on the side of the grids is purely a function of the aspect ratio, or cone of acceptance, for a given geometry. It is therefore obvious that density errors will be minimized for the flat grid, become larger for the woven grid, and become larger still for the double thick flat grid.

VI. CONCLUSION

Our simulation clearly demonstrates that grid geometry is an important factor in influencing the errors in inferred parameters in single retarding grid RPAs. Flat grids, woven grids, and double thick flat grids all show similar error structure in temperature, velocity, and density. These features are directly related to the departures from the ideal equation introduced by the structure of real grids. The thickness of the wire and the potential map between wires has a very noticeable effect on the inferred parameters. The woven geometry falls between the single flat grid and the double flat grid in terms of error magnitude for all inferred parameters, as expected due to its average depth. The errors predicted by earlier studies using models of flat grids must therefore be applied carefully to instruments that utilize woven grids.

The work presented here suggests that if a certain range of plasma temperatures is to be measured, then one grid geometry may have advantages over another. For any given mission a RPA could be designed using a retarding grid geometry that minimizes the errors in inferred plasma parameters based on the input temperatures and velocities that are expected for a given mission. The difference between the single thick and double thick flat grids also implies that by simply varying the grid depth, a region where relatively small velocity errors are produced can be achieved for a variety of input temperatures. This result, along with the fact that density errors are much larger for a double thick grid, should allow for even more optimization of instrument design in cases where measurement of one plasma parameter is deemed to be of higher importance than the others for a given mission. In typical ionospheric conditions (atomic oxygen, 800–2000 k) these results suggest that of the three geometries simulated here, a flat grid would provide the most accurate measurements for all parameters.

The next step in this study will include laboratory validation of the results presented here and more in-depth investigation of variation in flat grid geometries. Using an ion beam source and real grids in a vacuum chamber, it should be possible to ascertain how accurately these simulations reflect real instruments. Further simulation will also be carried out in hopes of determining an optimal aspect ratio for a flat grid to minimize errors for a given set of input plasma parameters.

ACKNOWLEDGMENTS

This work was funded by NASA Grant No. NNG06GH22G.

[1]E. C. Whipple, Proc. IRE **47**, 2023 (1959).
[2]H. Kil and R. A. Heelis, J. Geophys. Res. **103**, 407, doi:10.1029/97JA02698 (1998).
[3]W. B. Hanson, R. A. Heelis, R. A. Power, C. R. Lippincott, D. R. Zuccaro, B. J. Holt, L. H. Harmon, and S. Sanatani, Space Sci. Instrum. **5**, 503 (1981).
[4]F. J. Rich, *User's Guide for the Topside Ionospheric Plasma Monitor (SSIES, SSIES-2, and SSIES-3) on Spacecraft of the Defense Meterological Satellite Program, Volume 1: Technical Description* (Air Force Phillips Laboratory, Hanscome AFB, MA, 1994), p. 25.
[5]O. de La Beaujardiere and C/NOFS Science Definition Team, J. Atmos. Sol.-Terr. Phys. **66**, 1573 (2004).
[6]W. B. Hanson and F. S. Johnson, Planet. Space Sci. **40**, 1615 (1992).
[7]B. Tinsley, R. Rohrbaugh, W. B. Hanson, and A. Broadfoot, J. Geophys. Res. **102**, 2057, doi:10.1029/95JA01398 (1997).
[8]H. Bekerat, R. Schunk, L. Scherliess, and A. Ridley, J. Atmos. Sol.-Terr. Phys. **67**, 1463 (2005).
[9]S. Eriksson, M. R. Hairston, F. J. Rich, H. Korth, Y. Zhang, and B. J. Anderson, J. Geophys. Res. **113**, A00A08, doi:10.1029/2008JA013139 (2008).
[10]W. C. Knudsen, J. Geophys. Res. **71**, 4669 (1966).
[11]C. Chao and S. Su, Phys. Plasmas **7**, 101 (2000).
[12]C. Chao, S. Su, and H. Yeh, Adv. Space Res. **32**, 2361 (2003).
[13]J. H. Klenzing, G. D. Earle, and R. A. Heelis, Phys. Plasmas **15**, 062905 (2008).
[14]J. H. Klenzing, G. D. Earle, R. A. Heelis, and W. R. Coley, Phys. Plasmas **16**, 052901 (2009).
[15]D. A. Dahl, Int. J. Mass. Spectrom. **200**, 3 (2000).
[16]K. W. Morton and D. F. Mayers, *Numerical Solution of Partial Differential Equations. An Introduction* (Cambridge University Press, New York, 2005), pp. 50–54.
[17]G. E. Forsythe, M. A. Malcolm, and C. B. Moler, *Computer Methods for Mathematical Computations* (Prentice-Hall, Englewood Cliffs, NJ, 1977), pp. 159–170.
[18]D. W. Marquardt, J. Soc. Ind. Appl. Math. **11**, 431 (1963).